Article:

Watts, J. orcid.org/0000-0002-0411-8976 and Horoshenkov, K. orcid.org/0000-0002-6188-0369 (2025) Detecting defects in rising mains using the acoustic fluid velocity. Measurement, 253 (Part D). 117702. ISSN 0263-2241

https://doi.org/10.1016/j.measurement.2025.117702

Detecting Defects in Rising Mains using the Acoustic Fluid Velocity

It is a serious challenge to detect wall damage in live rising mains that transport wastewater along flat or elevated sections of the sewer pipe network. This work proposes a novel method that uses the acoustic velocity vector in the fluid to detect the onset of wall defects in a ductile iron rising main. Numerical simulations are performed to show that this acoustic velocity vector is more sensitive to the presence of a wall defect than the acoustic pressure or wall acceleration traditionally measured in fluid-filled pipes. The method can detect internal and external wall loss and small (0.020-0.025 m) wall perforations. An adapted triaxial accelerometer is used to demonstrate experimentally the method on an exhumed section of a 0.31 m diameter ductile iron pipe. It is shown that the radial and horizontal components of the acoustic velocity vector are particularly sensitive to the presence of small wall perforations. The proposed acoustic velocity sensor can be easily deployed on a mobile pipe inspection robot with a collocated or remote source of sound.

1. Introduction

Rising mains are used to transport wastewater uphill or along a long flat section of the network, where gravity is not sufficient and pumps are required. They are usually 0.1-1.0 m in diameter and designed to pump intermittently with up to 15 cycles per hour [1]. This intermittent loading, coupled with the fact that they are pressurised and filled with corrosive fluid mixed with solid sediment, makes them highly susceptible to damage.

Currently it is very challenging to inspect these pipes with a granularity suitable for detecting weak spots such as wall loss or small perforations. As a result, rising mains are left largely without any regular inspection, so bursts are only discovered when effluent reaches the surface. It may be a significant length of time from the partial failure of the pipe to full failure to the extent that its consequences are noticeable in this way. During this time the leakage is causing unnecessary pollution to the environment. It is highly undesirable in its own right and can lead to fines from the environment regulator. As such emphasis is being shifted from reactive to proactive defect detection. The ability to monitor the stages in this process in more detail from corrosion to failure would allow for much better planning of preventative maintenance and so a reduction in pollution. These stages have been formalised by Rizzo [2] in the form of the timeline towards the failure: a progression from a newly installed pipe, to a corroded pipe, to a partially then to fully failed pipe.

There are many ways in which rising mains can break. This failure is generally caused by either structural or internal deterioration, or a combination of the two [3]. Pipe failure can be broadly categorised into the following types of breaks [4]: circumferential cracking, longitudinal cracking, bell splitting, corrosion pitting, blow out hole, spiral cracking and bell shearing. To the best of our knowledge there has been very limited information on the performance of existing defect inspection and leak detection methods in relation to rising mains except one publication in the proceedings of the 2018 Water New Zealand Conference [5]. Good reviews of the capabilities and problems with the existing inspection methods in relation to pressurised clean water pipes can be found in Refs. [6, 7]. However, the authors struggled to find specific examples of these techniques being used on rising mains or objective assessment of their performance. The most relevant methods to this work are acoustic sensing using loggers, in-pipe pressure measurements and ultrasonic thickness measurements. Loggers [8] are placed on assets around the water network and listen to the acoustics on the outside of the pipe. This is a powerful tool to detect leaks in the clean water network. However, they need to be placed at least every 300 m on metallic pipes [9] or more frequently on plastic or large diameter pipes where the acoustic attenuation is much greater. They also assume that consistent measurements can be taken during the night, when genuine usage is at a minimum, this may make the technique difficult to adapt to rising mains given the highly cyclic nature of their use. They do not detect pipe wall thinning and small (background) leaks. In-pipe sensors such as Xylem's SmartBall [10], PipeDiver [11] and Sahara [12] systems use pressure and electromagnetic measurements to detect leaks. Xylem report these systems as being suitable for use on rising mains [13], but only a brief mention of somewhat successful surveys in 2012 could be found [14]. Ultrasonic sensors allow for detailed scanning of the pipe thickness, however they have a very short range, for example the pipeline inspection gauge (PIG) described in [15, 7] would require a full scan every 3 mm: this is impractical both from a timing and a data storage perspective particularly when applied to rising mains. Key issues with ultrasonic methods are the degradation and corrosion of the metal pipe wall, graphitisation and biofilms [6]. These inspection methods are relatively slow, rely on complex sensor arrays, complex signal processing methods and fast processing power.

This paper describes a novel method which allows for detection of incipient and existing leaks with a larger range than the current ultrasonic techniques, allowing for faster scanning of a pressurised pipe network when using a mobile in-pipe robot (or PIG). The paper also compares the efficacy of this sensor with using a hydrophone to measure the pressure. The proposed method is based on the measurement of the acoustic velocity vector excited in the fluid phase with a low-frequency remote source of sound. The acoustic velocity vector can be measured with a vector hydrophone or triaxial accelerometer suspended in fluid. It is shown through numerical modelling and laboratory experiment that the proposed method is very sensitive to the presence of even a small wall thickness loss. The method is based on low-frequency acoustics, using sound waves for which the wavelength is much greater than the diameter of the pipe. Low-frequency waves suffer less attenuation in buried pipes, allowing the acoustic velocity sensor to be effective over a longer range when deployed on a mobile robot moving away from a stationary source. This method has the potential to complete the inspection of pipe wall deterioration at a higher inspection rate over a longer section of a rising main or clean water pipe than any existing methods. This method is alternative to the emerging time reversal and matched-field processing methods, e.g. [16] - [18] that are based on measurement of the acoustic pressure at higher frequencies, multiple receiver positions and in a broader frequency range.

The paper is organised as follows. Section 2 presents the results of the numerical simulations. Section 3 presents the results of the laboratory experiment to validate the numerical simulations and to estimate the sensitivity of the proposed method. Section 4 presents the summary and conclusions from this work. There is an Appendix that examines the accuracy of the simulations performed in sections 2 and 3.

2. Effect of defects on an infinite pipe

2.1. A theoretical introduction

For waves with frequencies below the ring frequency, $f_r = c_p/(2\pi R)$, the fluid-borne waves are planar [19]. Here c_p is the speed of sound in the pipe material and R is the radius of the pipe. A planar wave travelling along the x-axis can be expressed in terms of pressure as

$$p(x,t) = p_0 e^{i(\omega t - kx)} \tag{1}$$

where $\omega = 2\pi f$ is the angular frequency, $k = \omega/c$ is the acoustic wavenumber in water and $i = \sqrt{-1}$ [20].

Extending this to find the net pressure, p_t, near a damaged region requires incorporating the acoustic field due to scattering from the defect p_s, so

$$p_t(x,y,z,t) = p(x,t) + p_s(x,y,z,t). \tag{2}$$

At low frequencies $|p_s| \ll |p|$ so it can be challenging to detect the presence of a defect using the pressure alone. If, instead, we consider the acoustic velocity

$$\boldsymbol{u} = \frac{\boldsymbol{\nabla p}}{i\omega\rho_f}, \tag{3}$$

with ρ_f as the density of the fluid, we can see that, combining equations (2) and (3), the total velocity in the y and z directions comes from the scattering defect, while the x velocity component is a combination of the planar and scattered velocities. The amplitudes of u_y and u_z are negligibly small in the pipe without a defect through the definition of the system provided in eq. (1). The presence of the defect in the pipe wall causes u_y and u_z to increase significantly, as it is illustrated in the following sections, to become measurable with a triaxial accelerometer suspended in the fluid or with an acoustic vector hydrophone. In order to determine the relative amplitudes of the velocities in each direction, and so the practicality of this as a method, the setup was studied numerically using COMSOL MultiPhysics, as described in the following section.

2.2. FEM setup

COMSOL Multiphysics [21] was used to create a finite element model to study the behaviour of the acoustic velocity and pressure in a ductile iron pipe with inner diameter 0.31 m and wall thickness 10 mm. These dimensions and materials are representative of a significant proportion of the rising main network and match the pipe available for the validation experiments described in Section 3. The length of the pipe in the model was set to 56 m to make it greater than the acoustic wavelength and to help control the reflections from the pipe ends while maintaining quick resolution times. Perfectly matched layers (PMLs) [22] were placed at each end of the pipe to minimise end reflections. The sound source was a planar pressure across the cross section of the pipe at -20 m from the defect (located at 0 m). The pressure on this plane was set to 600 Pa. The properties of the model are summarised in Table 1, while an analysis of the mesh chosen is provided in Appendix A.

Three pipe models were set up and run: (i) an intact pipe without any wall defects, (ii) a pipe with localized wall thinning to 1/3 of its normal thickness, (iii) a pipe with a wall hole of radius 0.01 m. In Figure 1 (a), the boundaries between the PMLs and the main pipe can be seen at each end, along with the defect at 0 m and the source plane at -24 m. A section of the mesh around the defects are shown in Figures 1 (b) and (c) for model configurations (ii) and (iii). In all of these models the frequency response to a planar pressure source operating at 170 Hz was considered. At this frequency the wavelength in water is approximately 8.6 m, considerably greater than the pipe's diameter of 0.31 m. The attenuation of sound at such a low frequency in a metal pipe is very small, i.e. $\alpha \ll 0.1$ dB/m (see Fig. 15 in [23]) and sound can travel well over 100 m with little or no attenuation (175 m is quoted on page 2764 in [23]). Therefore, the frequency of 170 Hz was selected based on the above evidence and field work conducted separately, which found that the pump noise in rising mains operates at approximately this frequency, future work aims to trial using the ambient pump noise as a sound source.

Table 1: The values of key parameters used in the COMSOL Multiphysics model for a ductile iron pipe.

Property	**Value**	**Unit**
Young's modulus	172	GPa
Poisson's ratio	0.275	-
Density	7150	kg/m^3
Length	56	m
Inner diameter	0.31	m
Wall thickness	10	mm

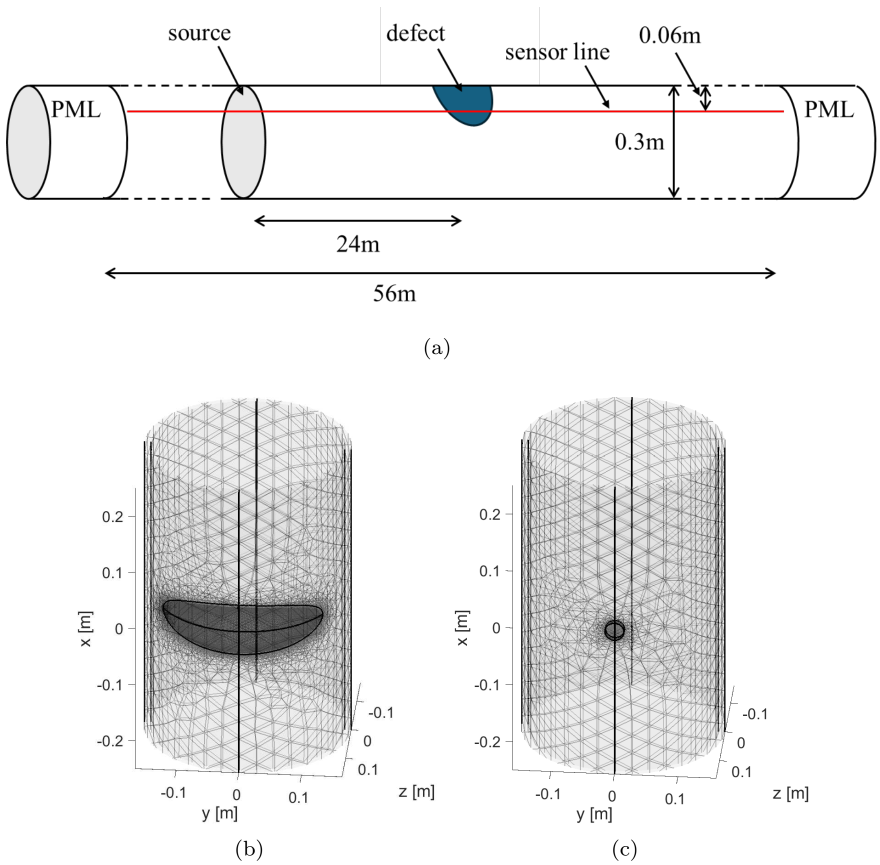

Figure 1: The model. (a) shows a schematic of the model, (b) and (c) show the mesh around the two defects modelled: thinning of the pipe wall and a hole in the pipe wall respectively.

2.3. FEM results

The amplitude and phase of the pipe wall acceleration, pressure in the fluid column and the acoustic velocity in all three axes were compared. This comparison is provided in Figure 2 for each of the three cases modelled, along with a quantitative comparison of the maximum difference caused by each type of defect for each parameter in Table 2. The acoustic pressure and velocity components shown were calculated along a line in the fluid offset 0.06 m from the defective pipe wall (this is the distance used in the experiment described in Section 3, and is shown in Figure 1 (a)).

The results presented in Figures 2 (a), (b) and (c) demonstrate that the wall

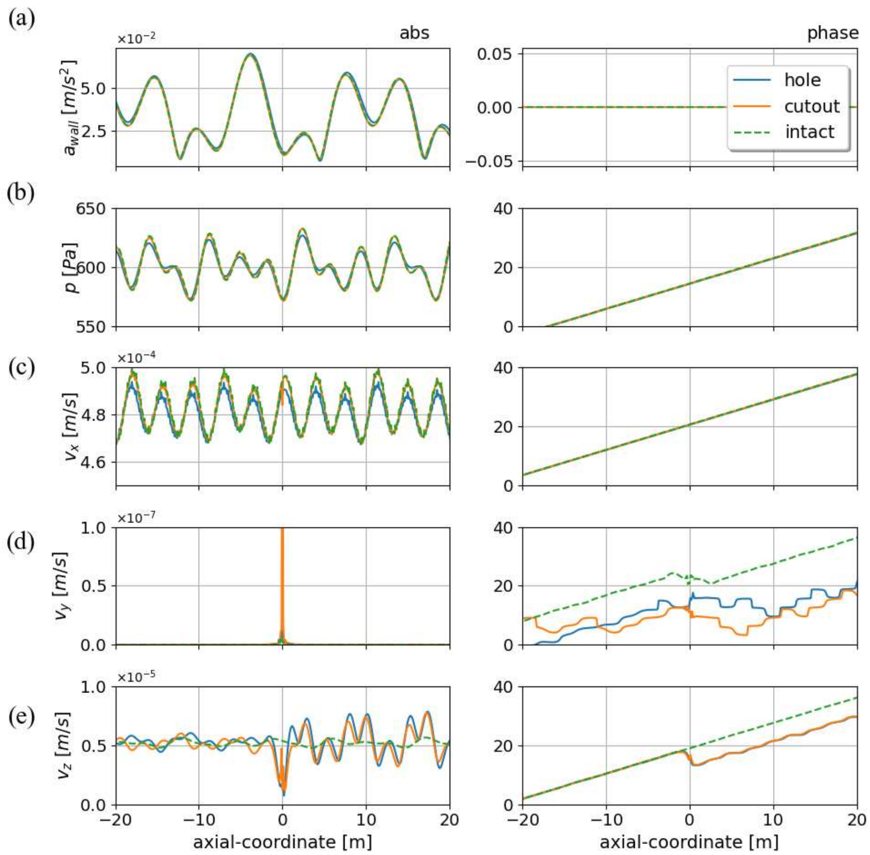

Figure 2: The results from the numerical simulation for sound propagation along an 'infinite' pipe with and without a defect. The amplitude and phase are shown for: (a) the wall acceleration; (b) the acoustic pressure; (c) the axial component of velocity (v_x); (d) the horizontal component of velocity (v_y); and (e) the vertical/radial component of velocity (v_z). The results in (b-e) are for a receiver line that runs 0.06 m from the edge of the pipe closest to the defect. The defect is at 0 m and the planar sound source is at -24 m.

Table 2: The maximum percentage change in the absolute value each variable, v, shown in Figure 2 for each type of defect. Calculated as the maximum difference in v along the axial coordinate divided by the maximum of v along that coordinate.

Defect	a_{wall}	p	v_x	v_y	v_z
Hole	5.0	0.7	0.4	410	45
Wall thinning	0.4	0.2	0.2	7800	37

acceleration, a_{wall}, acoustic pressure, p, and axial fluid velocity, v_x, are relatively insensitive to the presence of these defects. This can be seen in Table 2 where the maximum difference caused by a defect over the length of the pipe is less than 1% of the amplitude of each parameter in all cases except a_{wall}, where it is less than 5%. In contrast, the horizontal (torsional) fluid velocity, v_y, (Figure 2 (d)) shows a pronounced localised increase in its amplitude and much less localised change in the phase when a defect is present. Similarly, the amplitude of the vertical (radial) component of the acoustic velocity vector in the fluid, v_z (see Figure 2 (e)) shows a marked change in behaviour in the presence of a defect: its amplitude increases considerably and oscillates as a function of the axial position, x. While there is a phase shift in v_z downstream of the defect. The change in amplitude of v_z can be detected at a significant distance to either side of the defect, although it is again most pronounced downstream from the defect. The maximum percentage change in v_z due to a defect is significant: between 30 and 50% (see Table 2).

To understand better the behaviour of the pressure and radial velocities across the pipe, the amplitude of these quantities were plotted across a section of the pipe as shown in Figure 3. These plots show that the acoustic pressure (Figures 3 (a), (b) and (c)) is visibly unaffected by the presence of a defect across the entire width of the pipe so that it would be difficult or impossible to use this information to detect the wall thinning or perforation. On the other hand, the radial component of the acoustic velocity vector shows a clear change in its behaviour when the defect is present (Figures 3 (d) and (f)) as opposed to when there are no defects on the pipe (Figure 3 (e)). In the presence of the defect the symmetry of the system is broken in the entire region shown, and close to the defect there is strong increase in the velocity. This localised increase is different for the two defects, with the hole (Figure 3 (d)) showing a larger increase than the wall-thinning defect (Figure 3 (f)).

It should be noted that the described model does not account for the attenuation in the fluid and pipe wall.

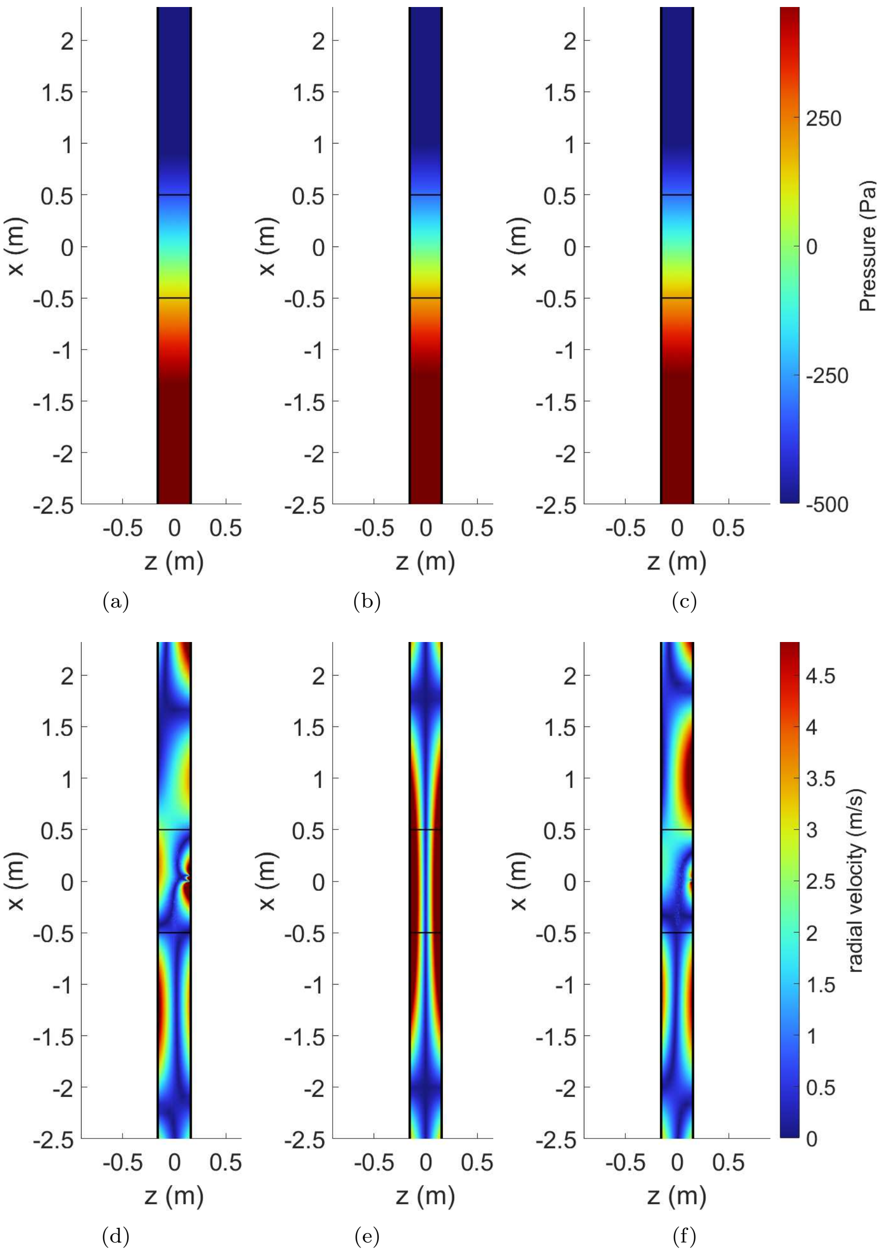

Figure 3: The results from numerical simulation for sound propagation showing the amplitudes of the acoustic pressure (a-c) and radial fluid velocity (d-f) for a cut plane through the middle of the pipe, showing 2.2 m to either side of the defect at 0 m. (a) and (d) the effect of pipe wall thinning. (b) and (e) pipe with no defect. (c) and (f) the effect of the hole in the pipe wall.

3. Experiments

Experiments were carried out to obtain data for numerical model validation and to demonstrate that the acoustic velocity is sensitive to the presence of a defect in the pipe wall. Measurements were conducted in a 2.0 m long, 0.31 m (internal) diameter ductile iron rising main exhumed for this purpose by Thames Water. As is common in rising mains, it exhibited significant deterioration of its bottom surface due to scouring. The pipe wall damage and its arrangement in the water tank are shown in Figure 4.

3.1. Methodology

The pipe was placed in water-tight PVC container (see Figure 4). The container was filled with water such that the pipe was fully submerged and covered with water 0.025 m above its crown. The relevant dimensions of the setup are included in Table 3. The same dimensions were used in the COMSOL model discussed in the following section to simulate the conditions of the experiment. An underwater speaker was installed in the centre of the pipe's cross-section at one end of the pipe. It was operated at 170 Hz to generate acoustic pressures of a few hundred Pascals. A wireless triaxial accelerometer was suspended with its centre at 0.06 m from the top of the pipe to measure the acoustic velocity.

The amplitudes of the axial, a_x, horizontal, a_y and radial, a_z, components of the fluid acceleration were measured and converted into the acoustic velocity components using the well-known relations $v_{x,y,z} = a_{x,y,z}/i\omega$. The results of the numerical simulations described in Section 2 suggested that for these acoustic pressures the accelerometer needed to be sensitive enough to detect accelerations of above 10^{-3} m/s^2 (or 9.36×10^{-7} m/s at 170 Hz in terms of the acoustic velocity). The accelerometer chosen for this work had a 20-bit resolution with range ± 2 g, giving a sensitivity of 4×10^{-5} m/s^2 (or 3.74×10^{-9} m/s at 170 Hz in terms of the acoustic velocity): more than adequate to detect the changes in the acoustic velocity field.

The triaxial accelerometer was installed in a 0.05 m diameter Perspex ball and suspended with rubber bands on a tensioned cable in the pipe as shown in

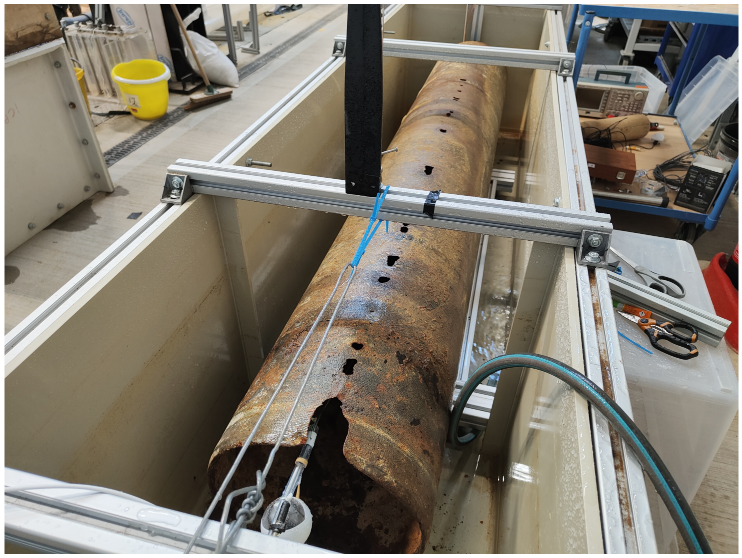

Figure 4: The experimental setup with a 2 m long, 0.31 m (internal) diameter ductile iron pipe in the ICAIR laboratory at Sheffield. The pipe has been inverted so its damaged surface is at the top.

Table 3: Key dimensions of the experimental setup. All distances are measured with respect to the start of the pipe and the bottom of the pipe (see Figure 7). The same parameters are used in the numerical model described in Section 3.2. The source pressure is measured at the speaker.

Property	**Value**	**Unit**
Pipe length	2	m
Pipe internal diameter	0.31	m
Speaker location	0.09	m
Speaker length	0.1	m
Source pressure	450	Pa
Tank start location	-0.156	m
Tank length	2.375	m
Tank height	0.473	m
Tank width	0.57	m
Tank wall thickness	10	mm
Frame height	0.118	m
Tank material	PVC	-
PVC Young's modulus	2.9	GPa
PVC Poisson ratio	0.4	-
PVC density	1760	kg/m3
Sensor elevation	0.25	m
Hydrophone elevation	0.3	m

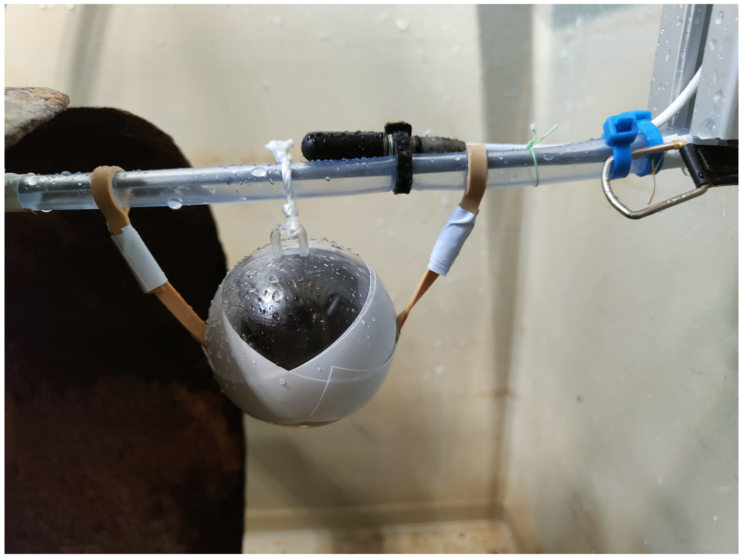

Figure 5: Sensor used for experiments.

Figure 5. This mounting method was chosen so as to encourage the accelerometer to vibrate under the influence of passing acoustic field along each axis independently and relatively unrestricted. In this way all the three acceleration components were detected and converted reliably into the acoustic velocity to validate the numerical model and to test the proposed pipe inspection method. The inherent shape of the accelerometer's enclosure was spherical to reduce acoustic streamline effects and to achieve a better match between the sensor and water densities. A hydrophone was mounted near the accelerometer to provide reference acoustic pressure measurements. These sensor arrangements are shown in Figure 5. The types of sensors and electronic equipment used in this experiment are listed in Table 4. Figure 7 presents a schematic view of the experimental setup, showing the relative positions of the sensor, speaker and pipe wall defect locations.

Measurements were taken for a range of sensor positions and pipe orientations. The position of the sensor was varied using a pulley system which moved the accelerometer along a wire 0.06 m from the top of the pipe. Measurements were taken across a 1 m range at 0.2 m increments to validate the model along

Table 4: The equipment used in the reported experiment.

Item	**Model**
Accelerometer	G-link-200
Hydrophone	B&K 8103
Hydrophone amplifier	B&K 2693-0S4 conditioning amplifier
Speaker	Visaton FR8
Speaker amplifier	Fosi Audio TDA7498E
Acquisition card	NI USB-4431

the pipe length and across a smaller 0.4 m range centred on a large defect at 0.025 m intervals to investigate the sensitivity of the sensor to defects as a function of distance from the defect. The angle between the sensor and the line of defects was varied by installing a wheeled frame under the pipe to enable accurate rotation of the pipe. This allowed the sensor to be exposed to both damaged and undamaged parts of the pipe's wall while moving the sensor along the length of the pipe. It also allowed for an investigation of the sensitivity of the sensor to the presence of a defect with respect to this pipe angle. Ideally the pipe would have been at 0 and 90° for the 'defect' and 'no-defect' cases, respectively. However, the geometry of the speaker prohibited measurements at those exact angles. Consequently the closest measurements to the defect were for a pipe angle of 9° and the farthest were for a pipe angle of 89°.

The signals from the accelerometer were sampled at the rate of 2046 Hz. It was not possible to synchronise the data acquisition from the accelerometer and hydrophone. Instead the hydrophone output was sampled and recorded independently at 12 kHz. The hydrophone data were then downsampled to match the recording frequency of the accelerometer data. The data from the two sensors were detrended and filtered in the frequency range between 140 and 200 Hz using a 4th order Butterworth filter to focus on the signal broadcast at 170 Hz. For each position a 5 s recording was taken, from which the average of the Hilbert envelope of the middle 1 s was calculated, to give a single amplitude for each location. This process has been summarised in Figure 6.

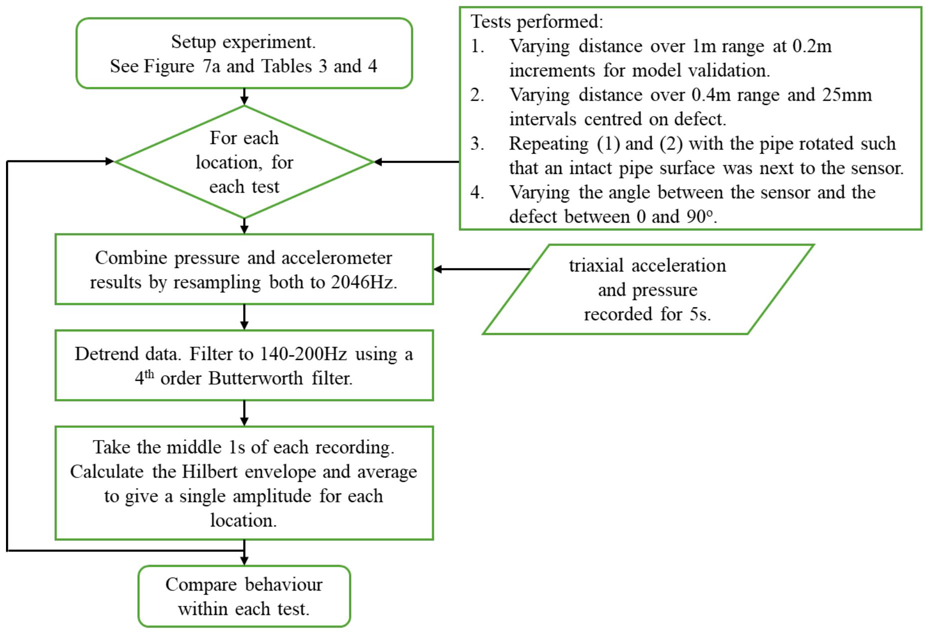

Figure 6: Flow chart of experimental process.

3.2. Numerical model of the experimental setup

Multiple consecutive defects in the pipe used in the experiment, the limited length of the pipe, the presence of the container and the free water surface caused acoustic distortions which meant that this setup did not reproduce the conditions in a typical, long rising main buried in soil. Consequently, direct comparison of the experimental data with the results of the original numerical model for an infinitely long pipe presented in section 2 was not possible.

A more representative numerical model was developed to simulate the multiple defects, finite pipe length, surrounding water and container response. This model is shown in Figure 7. The values of all the relevant parameters used in the model are provided in Table 3. The container walls were 10 mm thick PVC panels. Appendix A presents the validation of the mesh while Appendix B presents further results illustrating the sensitivity of the model to certain aspects of the environment, such as the container sides.

The results for the amplitude of the acoustic pressure and radial acoustic

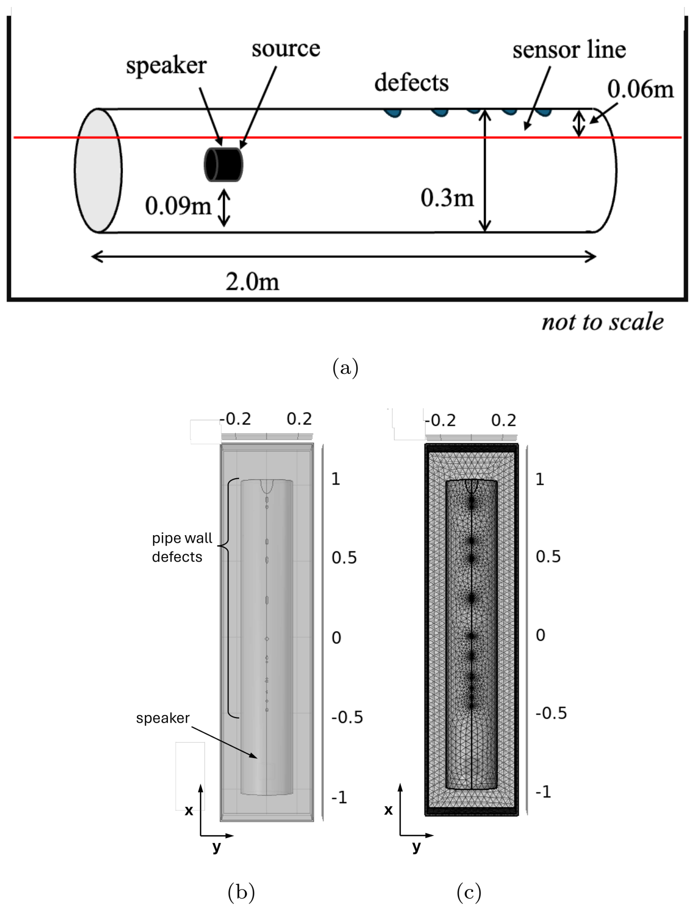

Figure 7: (a) schematic, (b) geometry and (c) mesh of model of pipe in PVC tank filled with water showing the locations of the speaker and pipe wall defects. The speaker has been modelled as an air filled metal cylinder, with the source face having a prescribed initial pressure. The location and size of the wall defects are based on the experimental setup, although they have been approximated as clean ellipses in the model. All the dimensions are in meters.

velocity predicted with the finite element model are shown in Figure 8. In Figures 8 (a) and (b), which show the results for the pressure, there is very little discernible difference between the pressure field for a pipe with defects along the top of the pipe (Figure 8(a)) and without (Figure 8(b)). In contrast, there is a clear change in the y and z velocity fields, as shown in Figures 8(c-f). v_x has not been plotted since it showed very similar behaviour to p. These results demonstrate that, as for the case of an infinite pipe, the acoustic velocity is at least an order of magnitude more sensitive to the presence of a defect than the acoustic pressure. A more detailed analysis of these results with reference to the experimental data is provided in Section 3.3.

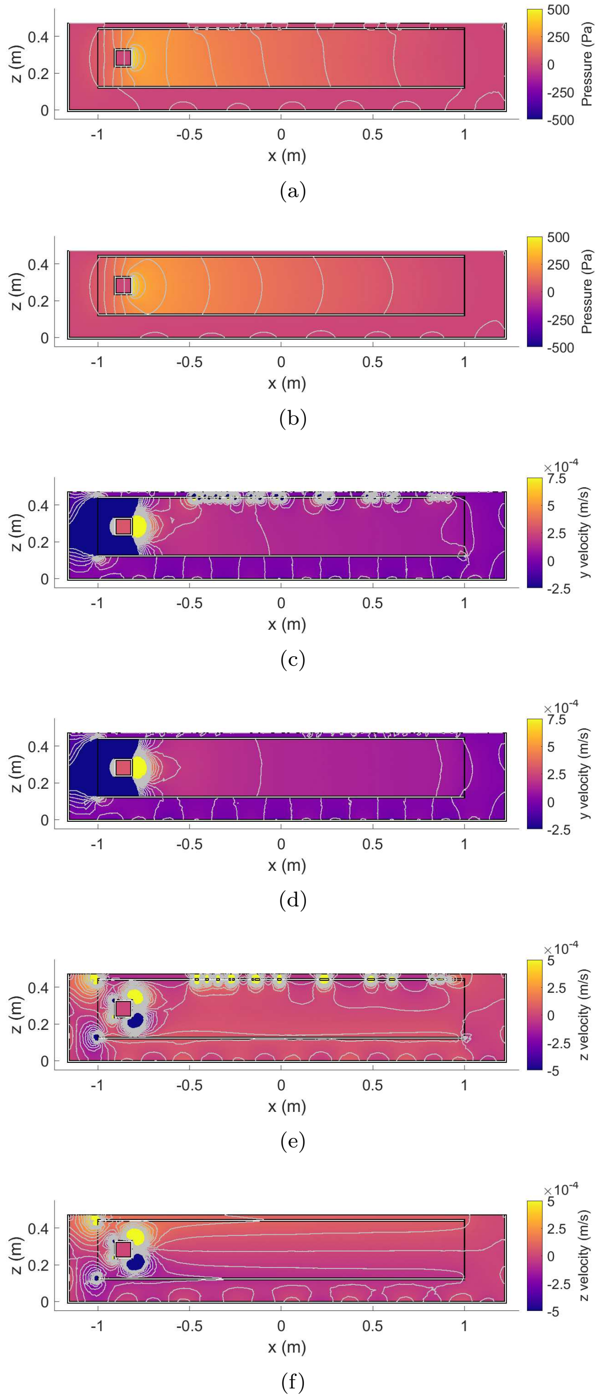

Figure 8: A comparison of the acoustic response of the fluid to a 170 Hz source positioned at x =-0.8 m, the response is shown for a vertical cut plane along the centre line of the pipe for (a, b) the acoustic pressure, (c, d) the horizontal component of the acoustic velocity vector and (e, f) the vertical velocity component. (a, c, e) show the acoustic response for a pipe with defects along its upper edge, (b, d, f) show the acoustic response for a pipe rotated by 90° such that the top edge is intact. The isolines are 50 Pa apart for the pressure graphs and 5×10^{-5} m/s apart for the velocity graphs.

3.3. Results

There are three sets of results presented in the following sub-sections. The first set aims to compare the numerical model against experimental data taken over a 1 m length of pipe centred 1.3 m from the end of the pipe. The second set presents data and their variability in close proximity to a defect between 1.025 and 1.425 m. It also presents a comparison with the results of the numerical simulation in this region, thereby supporting the veracity of the observed behaviour of the acoustic pressure and velocity. Finally, the angular dependence of the acoustic velocity measured along the pipe's circumference is studied for two different axial locations in order to assess the sensitivity of the method to orientation.

3.3.1. Model calibration

In order to evaluate the accuracy of the model, measurements were taken at 0.2 m intervals along the length of the pipe. To study cases close to and distant from defects (see Figures 4 and 7), the pipe was rotated to move the line of defects closer to or further away from the sensor. In this experiment the two cases were realised with the pipe rotated to 9° and 89°, respectively. A comparison of the results of the model and the experiment is provided in Figure 9 for the acoustic pressure measurements and for the three components of the acoustic velocity vector. The amplitude of the each acoustic velocity component was normalised by the acoustic pressure amplitude measured at the same time. This removed drift observed in the speaker output.

There are strong similarities in the behaviour of the measured and modelled velocities near and away from the line of defects. However, the measured acoustic pressure is significantly lower than that predicted close to the speaker. It is believed that this is due to the speaker overheating occasionally during testing causing a drift in output. For both of these sets of measurements the data shown was recorded at 1.8 m first, and the sensor moved along the pipe to 0.8 m with only small gaps between tests. The acoustic velocity measurements have been normalised by the pressure to remove this effect. Aside from the drift in

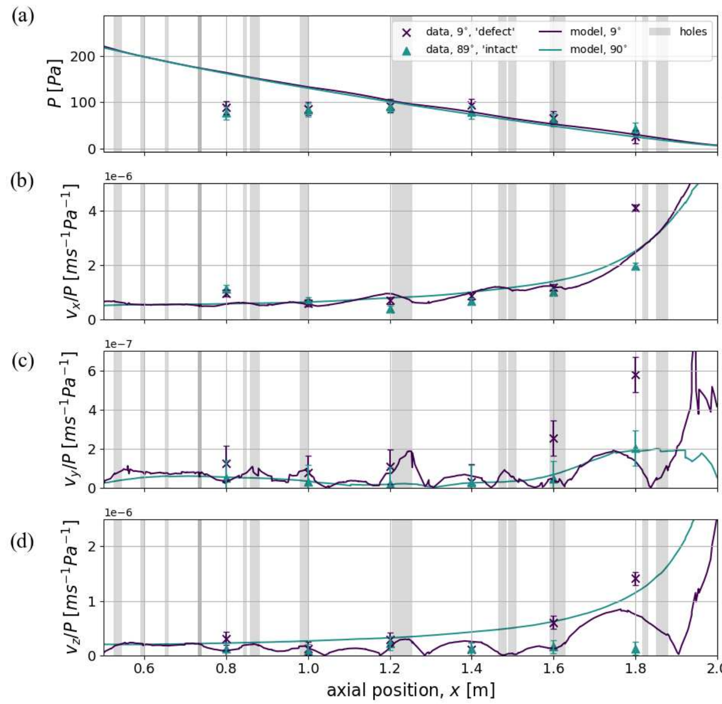

Figure 9: A comparison of the measured (markers) and modelled (lines) acoustic quantities. The error bars are calculated as the standard deviation of 2 x 9 repeated measurements on an intact and defective section of pipe. The location of the holes are indicated by the shaded regions in gray. The green Δ markers and lines are the results corresponding to the receiver being next to intact pipe wall. The purple $\times$ markers and lines are for the results corresponding to the receiver being next to the defects.

amplitude, the measured pressure are very similar for the two pipe orientations, as expected based on the model. For the first few measurements, from $x = 1.6$ to 1.8 m the amplitude of the measured and predicted pressures are also very similar.

The axial component of the acoustic velocity, v_x, displays the most similarities between the modelled and measured data, with the dominant behaviour being a clear increase in amplitude along the length of the pipe. The measurements of v_x have a variability (as measured by repeating measurements 9 times at two locations and calculating the standard deviation) of 1.2×10^{-7} m/s/Pa. Given this level of error there is little difference between the axial velocity measured in the presence or absence of the defects, i.e. v_x is relatively unaffected by the presence of the defects.

In contrast, a key influence of the line of defects on the acoustic field in the pipe is a much more complex variation in the horizontal and radial components of the acoustic velocity (v_y and v_z) when compared to the case where the sensor is close to an 'intact' section of pipe. The predicted acoustic field close to the defects shows localised increases in v_y and v_z, wherease next to an intact pipe the acoustic field is smooth along the pipe length. The horizontal component of the acoustic velocity vector, v_y, is very sensitive to the proximity of the line of defects (compare the purple line versus the green line in Figure 9(c)). The agreement between the model and experiment deteriorates for $x > 1.6$ m, with the maximum difference of 4.3×10^{-7} m/s/Pa between the model and data at $x = 1.8$ m corresponding to a relative error of 300%. It should be noted that the amplitude of v_y is at least an order of magnitude smaller in comparison with that measured for v_x and v_z, this may make it challenging to measure v_y outside of a lab environment, in areas with higher background noise.

The predicted radial component, v_z, of the acoustic velocity also shows a close agreement between the experimental data and the model for the case when the line of defects was near the sensor and for $x \leq 1.6$ m. For $x > 1.6$ m the measured amplitude of the radial velocity component is significantly larger than predicted. For most of the measured range, the model over-predicted the amplitude of the radial velocity component for the case when the sensor is away from the line of defects. The discrepancy is particularly acute for $x > 1.6$ m, where the measured velocity has remained constant but the model predicts an increase towards the end of the pipe.

The consistent discrepancies between the model and data towards the end of the pipe may be due to the increasing deterioration of the pipe condition in that region such that the model is a poor representation the conditions: the model has assumed that the edges of defects are smooth, it can be seen in Figure 4 that this is not always the case. Further, the model assumes the internal walls are smooth and of consistent thickness, in fact ultrasonic gauge measurements show that the pipe wall thickness varied from 10.6 to 11.9 mm. Finally, the walls of the water tank caused a large number of reflections resulting in a complicated pattern of standing waves. A summary of investigations into this complexity is provided in Appendix B.

3.3.2. Acoustic field near a defect and measurement repeatability

A more granular set of measurements was taken at 0.025 m increments over a 0.4 m range around a 0.05 m diameter hole (the defect) at 1.225 m in order to determine how sensitive the acoustic pressure and velocity vector components are to the presence of the defect. The measurements were supported with COMSOL simulations to determine the ability of the model to reproduce the fine structure of the acoustic field in the vicinity of the defect. The results are shown in Figure 10 for the sensor installed at 9° (near the defects) and 89° (away from the defect). As in Section 3.3.1, the three velocity components shown in Figures 10(b-d) were normalised by the amplitude of the corresponding pressure measurement. The data in this figure are presented with error bars showing the variation in measurements over 3 repeats at each location.

The analysis of the measured and predicted acoustic pressures shown in Figure 10(a) suggests that this quantity is insensitive to the presence of the defect. The predicted amplitude of the acoustic pressure reduces with distance from the speaker. This behaviour is not supported with the measured data which are relatively independent of the distance.

The analysis of the measured and predicted acoustic velocities shown in Figures 10(b-d) for the amplitude of the three components of the acoustic velocity vector suggests that the model captures well the general behaviour of the measured data at 9°. The maximum relative error is 220% for the data at 9° (for v_z at $x = 1.402$ m).

The defect has a relatively small effect on v_x, in line with the modelled result (see Figure 10(b)). The horizontal component of the acoustic velocity, v_y, is sensitive to the presence of the defect as shown in Figure 10(c). The data show that its amplitude displayed a sharp local change by a factor of 7 when the sensor was placed close to the defect. The model captures particularly well the

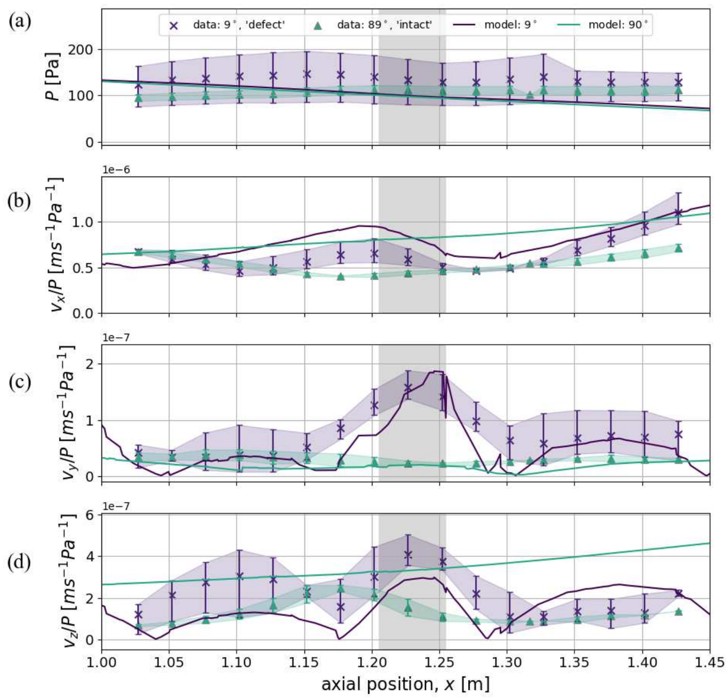

Figure 10: A comparison at a higher resolution of the measured (markers) and modelled (lines) acoustic quantities around a 0.05 m hole at $x = 1.225$ m (the shaded region in gray). The green Δ markers and lines are the results corresponding to the receiver being next to intact pipe wall. The purple $\times$ markers and lines are for the results corresponding to the receiver being next to the hole. The error bars show the repeatability of measurements.

behaviour of v_y with the maximum relative error being 120% at $x = 1.252$ m for angle 9° and the mean relative error being 46%. For this component of the acoustic velocity the model is mostly within the experimental error both near the defect and away from the defect. In the case when the sensor is away from the defect, the behaviour of the model and data is much less complex and relatively independent of the distance.

Similar behaviour can be observed in the v_z data, with the measurements and predictions close to the line of defects showing much more variation than the modelled intact case. The measurements of the ‘intact’ pipe deviate strongly from the model here, and show more variation across this length than might be expected. There is also more of a discrepancy between the modelled and measured values of v_z close to the defects for $x < 1.15$ m and $x > 1.30$ m (up to a relative error of 220% at 1.402 m for 9°). There are two possible reasons for these differences. Firstly, the thickness of the pipe was not constant. The level of corrosion and graphitisation in the pipe material was not known. The pipe wall thickness was measured for points on the wall corresponding to each of the data points shown in Figure 10. Over this range the pipe wall thickness varied by 1.3 mm with the average being 11.2 mm. Also, the results shown in the Appendix suggest that the effect of the tank wall can be rather complex to capture accurately with the proposed model because the predicted acoustic pressure and velocity components are dependent on the choice of the Young's modulus for the PVC panel material and the quality of the tank assembly.

3.3.3. Effect of pipe angle

When scanning a pipe in a laboratory or in the field there is no guarantee that the sensor will be aligned perfectly beneath any defects, i.e. within a given pipe cross-section there may be some angle between the defect line and the sensor. An additional experiment was carried out to determine the effect of this pipe angle on the amplitude of the three velocity components measured with the tiaxial accelerometer. The results from this experiment, shown in Figure 11 and summarised in Table 5, suggest that the horizontal component of the acoustic velocity vector is the most sensitive to the angle at which a defect is approached. The amplitude of this component increases progressively when the angle reduces below 40° (see 11(b)). A 5.5-fold maximum increase in the amplitude is observed in the v_y data when the sensor was at 9°. The behaviour of the amplitude of the radial velocity component as a function of pipe angle is more complicated as illustrated in Figure 11(c). The maximum v_z amplitude is for the minimum angle of 9°. It is a 3-fold increase with respect to that recorded at 89° and it is approximately 2.5 times greater than the maximum of v_y at 9°. Between these angles v_z oscillates suggesting that it can be possible to use this quantity as an indicator of the wall damage presence even if the sensor is not in the immediate vicinity of it, e.g. at 40-50°. In contrast, the angle has little

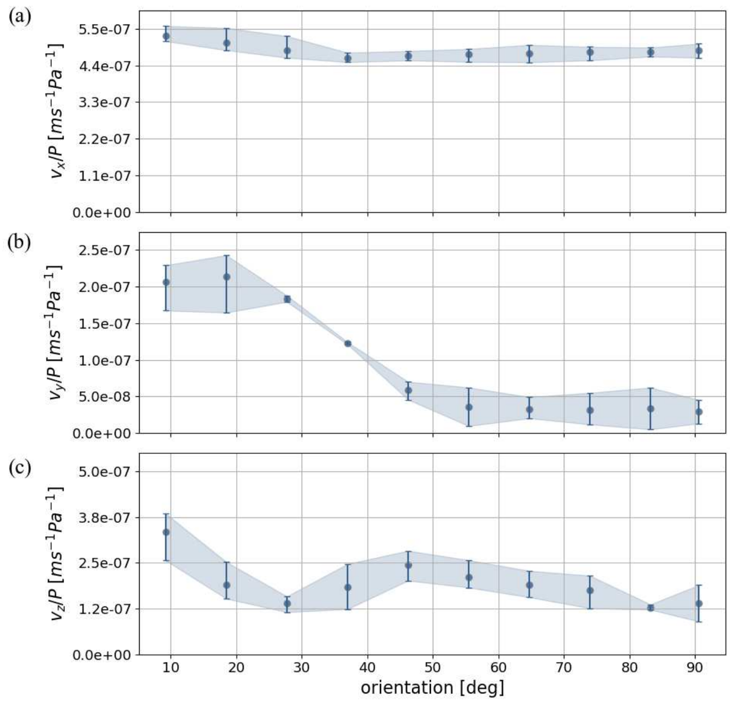

Figure 11: The effect of the angle between the sensor and line of defect on the amplitude of the three components of the acoustic velocity vector. The data were taken at $x = 1.227$ m, corresponding to the pipe cross-section with a 0.025 m diameter hole at 0°.

effect on the amplitude of the axial component of the acoustic velocity, v_x (see Figure 11(a)). There is still some increase in v_x when the angle reduces from 89° to 9°, but its amplitude does not change by more than 16% confirming that this velocity component is much less sensitive to the presence of damage.

Table 5: Summary of variation in each parameter over angle, in x10^{-7} m/s/Pa.

	Max.	Angle	**Min.**	Angle	Change
v_x/P	5.3	9.24	4.6	36.97	14%
v_y/P	2.1	18.48	0.29	90.56	150%
v_z/P	3.3	9.24	1.3	83.17	90%

3.4. Discussion and future work

This paper has demonstrated both numerically and experimentally that the acoustic velocity in a low frequency sound wave is a much more sensitive to the presence of a pipe wall defect than the acoustic pressure. A new acoustic velocity sensor based on a high-fidelity triaxial accelerometer has been designed and tested in a 0.31 m diameter, 2 m long water-filled ductile iron pipe with wall perforations and wall thinning representing typical in-pipe defects. The sensor has been suspended in water to respond freely to the passing sound wave. This pipe used to serve as part of a rising main to pump wastewater. A refined COMSOL finite element model of this pipe placed in a water-filled tank has been developed to predict the acoustic pressure and velocity distribution. The model has been validated against the data from a complementary laboratory experiment. It has been shown that the model agreed with the data within certain regions; the error increases to 220% in the worst case, where end effects and simplifications in the defect shapes are most egregious. For the central region of the pipe, the model agrees with the measured data to within 20%, and the trends in behaviour are very consistent between the two.

The results from the numerical simulation for a long rising main suggest that the radial and horizontal components of the acoustic velocity vector are very sensitive to the presence of wall damage such as wall thinning or perforation. These results (see Figures 10 and 3) demonstrate that the presence of a defect in a long water-filled pipe has a profound influence on the amplitude of the horizontal (tangential) and vertical (radial) components of the acoustic velocity vector. This influence can be detected many meters away from the defect. The distance at which this defect can be detected is much greater than the defect's dimensions.

The results of our experiment in the 2 m long water-filled section of an exhumed rising main suggest that the proposed acoustic velocity sensor can very clearly localise a 0.025 m diameter defect at around 0.1 m away from it (see Figure 9) and within an angular range of 9-40° (see Figure 11). The method has used a scanning resolution of 25 mm, as opposed to the 3 mm used by the

PIG in [15, 7], allowing for significantly faster scanning of the pipe than would be possible with this PIG. It has been confirmed from the experiment that the acoustic pressure and axial velocity components are relatively insensitive to the presence of pipe wall damage. On the contrary, the radial and horizontal components of the acoustic velocity are very sensitive to wall damage. It has been shown that the amplitude of these two components changes by up to a factor of 5 when the sensor and damage spot were aligned.

This finding suggests that the new sensor offers the opportunity to detect damage in live rising mains and clean water pipes made from ductile iron. The presence of pipe wall damage is clearly visible in the acoustic velocity data much further away from its centre than the damaged spot dimensions. This sensor can be deployed on an in-pipe robotic platform, allowing for detection of significantly smaller wall defects than is currently possible. The use of low-frequency sound waves with relatively low attenuation in metal pipes enables the sound source to be placed far away from the sensor making it easier to control the experiment, quality of the collected data and to manage power.

The next stage of this project will look at deploying this sensor on an autonomous robot roaming a long section of a buried rising main. A limitation of the work presented here is that reference measurements of the pipe are required, since the presence of a defect is decided based on comparison with the baseline. Therefore, part of the future work will be to investigate whether acoustic information collected continuously while traversing from an intact pipe section to a defective section can be used to train a suitable machine learning algorithm to detect the defect, or whether reference measurements of an exemplary pipe are still required.

4. Conclusions

In this paper the efficacy of a triaxial accelerometer at detecting a small defect in the wall of a rising main has been demonstrated. The difference between measurements taken close to a defect and those next to an intact section of pipe is within the limits of the repeatability of the sensor measurements, and the deviation in behaviour close to a defect is striking enough to be detectable in a scan along the pipe length. This result has been proven experimentally in a limited setting, for the specific case of small holes in a pipe wall. It has been used to validate the results of numerical models which predicted that the radial and torsional components of the acoustic velocity would be more sensitive to small defects in a pipe than the pressure or axial velocity. These models go beyond the results of the experiment and predict that the acoustic velocity vector can be used to find not only small holes in the pipe wall, but also internal and external pitting defects. Further work is required to investigate the limitations of this result experimentally, although the range of the sensor in terms of axial distance from a defect and angle between the sensor and the defect has been shown. This work stands as a proof of concept that this kind of sensor can be used to detect small defects in pipe walls, allowing for improved predictive and preventative maintenance of pipes.

5. Acknowledgements

This work is supported by the UK Engineering and Physical Sciences Research Council (EPSRC) Programme Grant EP/S016813/1. The authors would like to thank Mr. David Walters of Thames Water for kindly providing an exhumed section of rising main used in the reported experiment. The authors would also like to thank our technician, Mr. Paul Osborne, for kindly helping with the design of the water tank and installing carefully in it the exhumed pipe section. Finally, the authors would like to thank Mr. Gavin Sailor for helping with LabView software used in this work for data acquisition. For the purpose of open access, the authors have applied a 'Creative Commons Attribution (CC BY) licence to any Author Accepted Manuscript version arising.

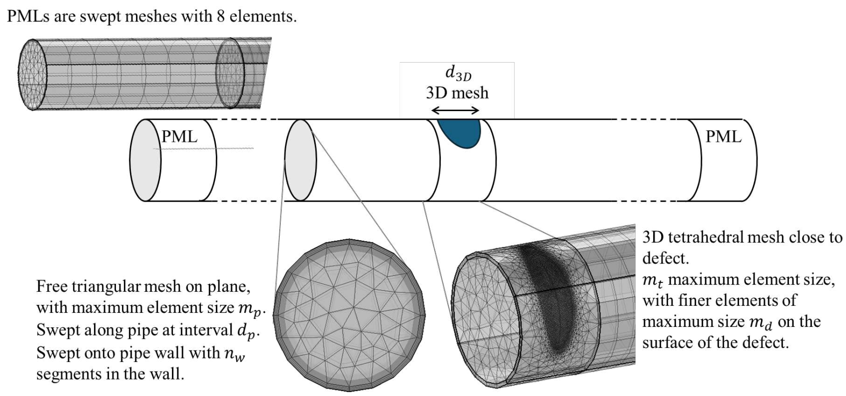

Figure A.12: Schematic of the mesh for the model described in Section 2.

Appendix A. Model development: mesh validation

In order to understand better the accuracy of the finite element models described in Sections 2 and 3.2 the size of the meshes in each model was varied and results analysed accordingly

Appendix A.1. Validation of basic model

A schematic view of the mesh used in the model described in Section 2 is provided in Figure A.12 showing each of the meshing elements. Based on this there are 6 main parameters than can be modified within the mesh:

- m_p, the maximum element size of the free triangular mesh that is swept along the majority of the pipe.
- d_p, the distance between elements in this swept mesh.
- n_w, $n_{w,3D}$, the number of elements in the pipe wall, in the main pipe wall and close to the defect (in the 3D section).
- m_t, the maximum element size of the tetrahedral mesh close to the defect.
- m_d, m_h, the maximum element size on the surface of the defect/at the location of the hole in the pipe.

Table A.6: A representative selection of the mesh sizes tested for basic model, where R is the radius of the pipe, h is the pipe wall thickness and r is the radius of the hole in the pipe wall.

m_p, m_t	d_p (m)	n_w	$n_{w,3D}$	m_d	m_h	d_{3D} (m)	description
$R/2$	0.3	1	3	h	r	1	very coarse
$R/3$	0.25	1	5	$h/3$	$r/3$	1	coarse
$R/5$	0.25	2	7	$h/4$	$r/5$	1	medium
$R/8$	0.2	3	10	$h/4$	$r/8$	1	ultra-fine
$R/3$	0.25	1	5	$h/3$	n/a	2	fine, long 3D
$R/8$	0.1	5	5	$h/4$	$r/8$	0.25	med., short 3D

- d_{3D}, the length of the 3D mesh.

In order to simplify the problem, we set $m_p = m_t$ in all cases.

The size of the mesh used in each test for each section of the model is summarised in Table A.6, with the results compared in Figure A.13. The error here is calculated as $\epsilon = (x_{model} - x_{fine})/(x_{fine} + \zeta)$, where ζ is a regularisation constant and x_{model} and x_{fine} are the feature of interest for the model under consideration and the model with the fine mesh, respectively. It can be seen that the error in the results is similar for both the medium and fine meshes, however the fine mesh has lower errors close to the defect for p and v_x, so was chosen for the model described in the main text. The results along the length of the pipe for each parameter are shown in Figure A.14 for a subset of the mesh sizes shown above. The relative error as a function of the mesh size is also shown. Inspection of Figure A.14 shows that the relatively high error in v_y is dominated by a very dissimilar result immediately next to the defect, removing this increases the similarity in the results of the fine and ultra-fine meshes, the remaining high relative error can be explained by the very low values of v_y being measured. There is a similar very localised increase in the error of v_z close to the defect, largely due to the sudden decrease in v_z distorting the error calculation. In general the low level of difference seen between the fine and ultra-fine meshes led to the selection of the fine mesh for the results presented in this paper.

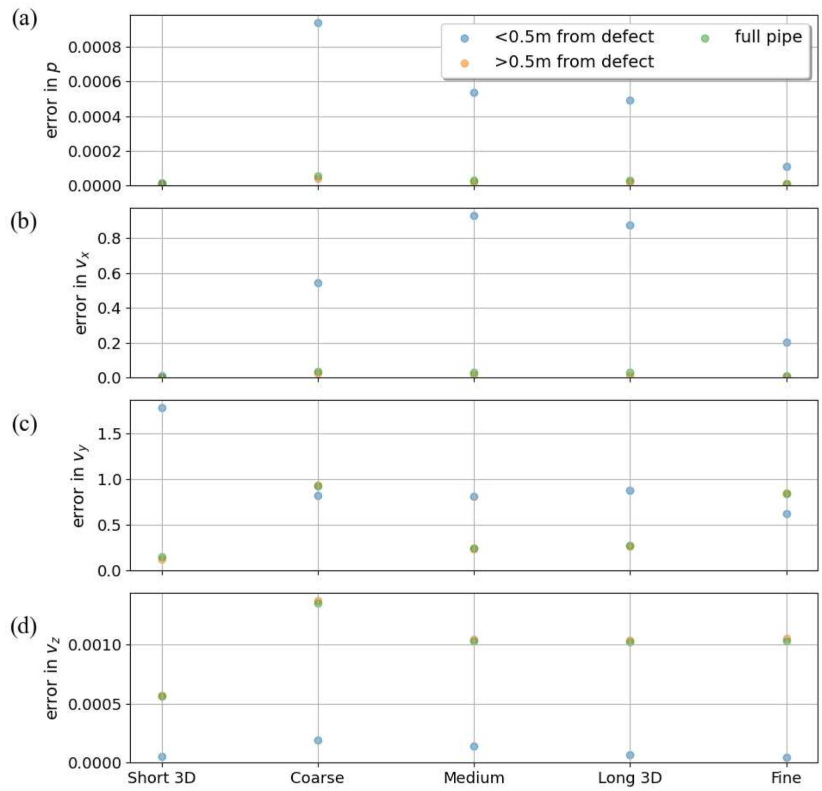

Figure A.13: Effect of different sized meshes on the error in the value of each parameter along the sensor line. The error has been calculated with respect to the 'ultra-fine' model. The mesh sizes for each section of the model are summarised in Table A.6.

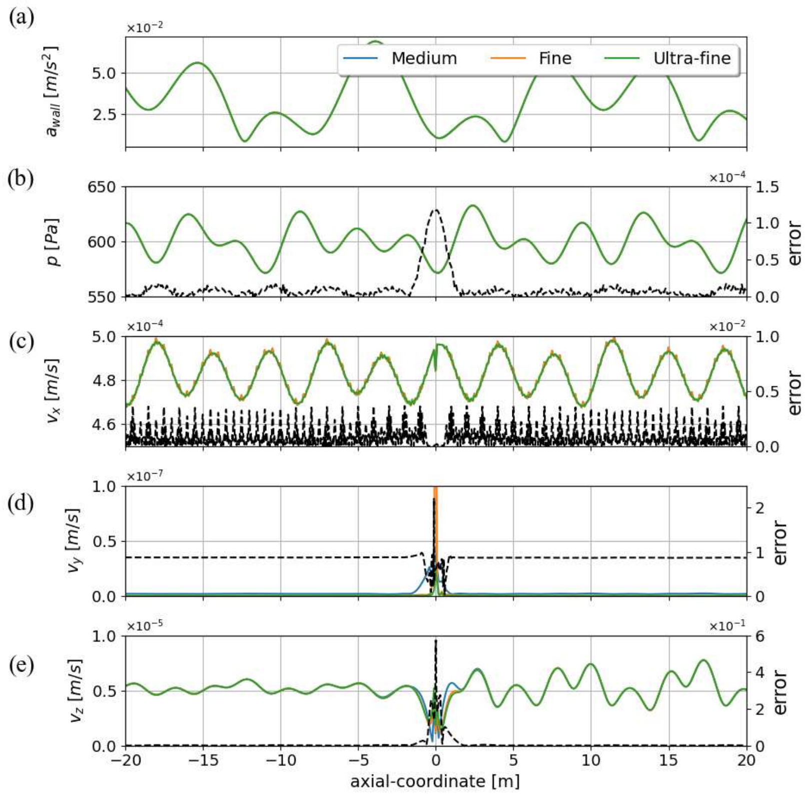

Figure A.14: Effect of different sized meshes on the model results along the sensor line for 3 different meshes. The error is between the fine and ultra-fine meshes. The mesh sizes for each section of the model are summarised in Table A.7.

Table A.7: The maximum element size, in m, for the mesh in each component in the model.

Component	Mesh used	Finer mesh
tank	0.25	0.05
pipe wall	0.25	0.01
pipe interior	0.25	0.01
speaker	0.08	0.01
defect	0.005	0.001

Table A.8: The relative error between the fine mesh and that used in the final model.

Pressure	v_x	v_y	v_z
0.078	0.057	0.038	0.048

Appendix A.2. Validation of model mesh of experiment

This section provides a comparison between the model used in Section 3.2 and a significantly finer mesh (for context the model used take 2.5 minutes to run, the finer meshed model takes 6 hours). The maximum element size of each component of the model for the two cases is provided in Table A.7.

The relative error, ϵ, was calculated for each of the parameters of interest, and is shown in Table A.8. These are relatively high, however an inspection of the relevant graphs (Figure A.15) shows that the main contributions to these errors are close to the speaker and at minima in the signals. An inspection of Figure A.16 further demonstrates the strong similarities in the behaviour of the two models. This led to the choice of mesh used.

(a)

(b)

(c)

(d)

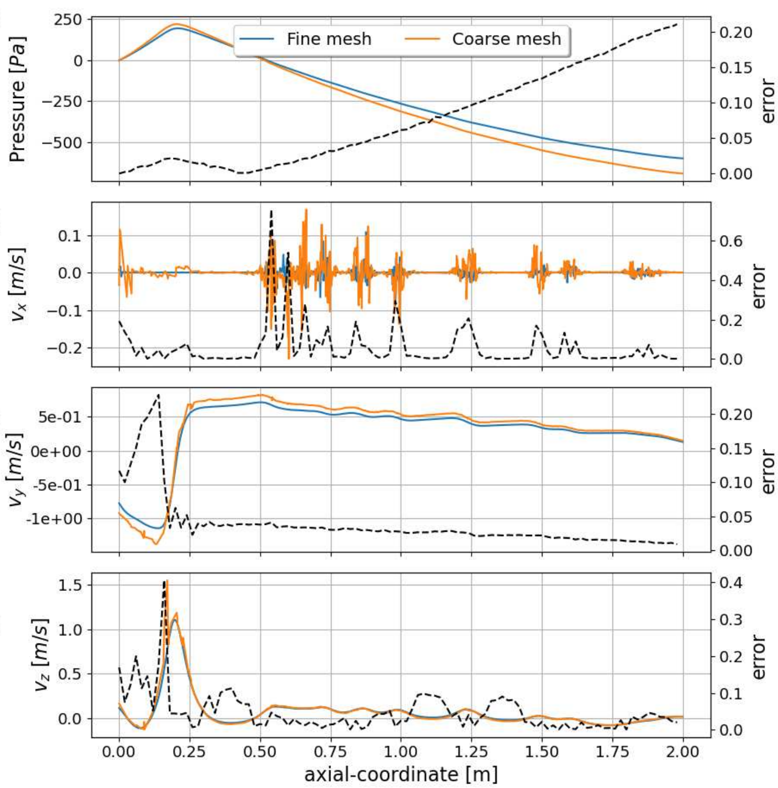

Figure A.15: Effect of different sized meshes on the model results. The mesh sizes for each section of the model are summarised in Table A.7.

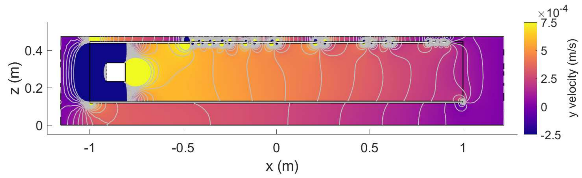

(a)

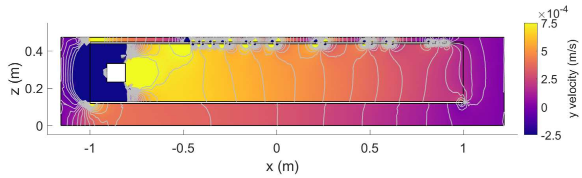

(b)

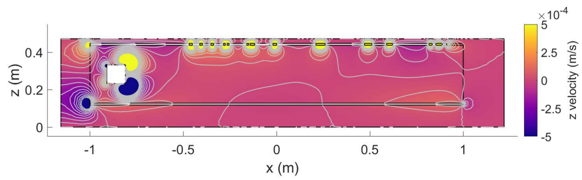

(c)

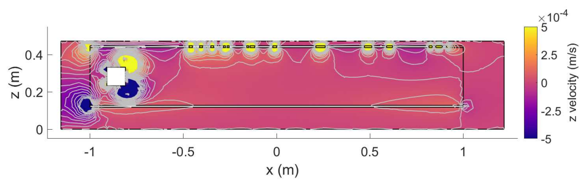

(d)

Figure A.16: A comparison of the acoustic response of the fluid to a 170 Hz source positioned at x =-0.8 m, the response is shown for a vertical cut plane along the centre line of the pipe for (a, b) the horizontal component of the velocity and (c, d) the vertical component. (a) and (c) show the results for a fine mesh, while (b) and (d) show the results used in the main body of this work. The isolines are 5×10^{-5} m/s apart.

Appendix B. Model development: parametric analysis

The water level in the tank and visco-elastic properties of PVC panels of which the tank was made are two parameters that may affect the acoustic pressure and velocity predicted with the COMSOL model. An investigation into these effects were carried out accordingly. In this investigation:

i) the Young's modulus of the PVC panels was varied from infinitely rigid, as assumed in the original model, to $E = 2.9$ GPa and 4 GPa, respectively;

ii) the depth of the water in the tank was varied from its base value of 0.025 m to 0.1 m, 0.25 m and 0.5 m above the crest of the pipe, respectively.

The results of these permutations were compared against those from the 'baseline' model presented in the main body of the paper. The geometry of the model was not varied from that shown in Figure 7 and detailed in Table 3. Figures B.17 and B.18 present the results that illustrate the effect of the finite Young's modulus for the PVC panels and water level in the tank, respectively. The solid lines shown in these figures correspond to the case with the pipe wall perforations. The dashed lines correspond to the case of the undamaged pipe. The velocity amplitudes were normalised by the acoustic pressure to support a comparison with the results shown in the main body of this paper.

It can be seen in Figures B.17 (a,b) that changing the Young's modulus of the PVC panels has a minimal effect on the amplitude of the acoustic pressure and axial velocity component. However, the finite value of the Young's modulus has a much more pronounced effect on the horizontal (Figure B.17 (c)) and radial (Figure B.17 (d)) components of the acoustic velocity particularly as the receiver approaches the source. Generally, there is a significant, approximately 2-fold, increase in the amplitude of the radial velocity in the case when the walls of the tank are acoustically rigid. The behaviour of the horizontal component of the acoustic velocity is more complex and somewhat chaotic. The difference between the results for $E = 2.9$ GPa and $E = 4.0$ GPa are very small. This difference is much larger between the case when the tank panel is assumed rigid and when it is elastic, i.e. when the value of E is finite.

Figures B.18 demonstrate the effect of water level on the four acoustics quantities. In these calculations the tank walls were assumed rigid. The acoustic velocities were normalised again by the acoustic pressure to support a comparison with the results shown in the main body of this paper. These results suggest that the effect of the water level on the acoustic pressure is relatively small (see Figure B.18(a)), but stronger than the effect of the value for E (see Figure B.17(a)). Generally, the acoustic pressure amplitude slightly increases by a few % with the increased water level. The effect of water level on the amplitude of the three acoustic velocity components is also small, except at distances farther away from the speaker and near the far end of the tank (see Figures B.18(b-d)). For example, the normalised amplitudes of v_z/p can vary by up to a factor of 2 at $x = 1.8$ m (see Figure B.18(d)). Generally, amplitude of the acoustic velocity components decreases with the increase in the water level.

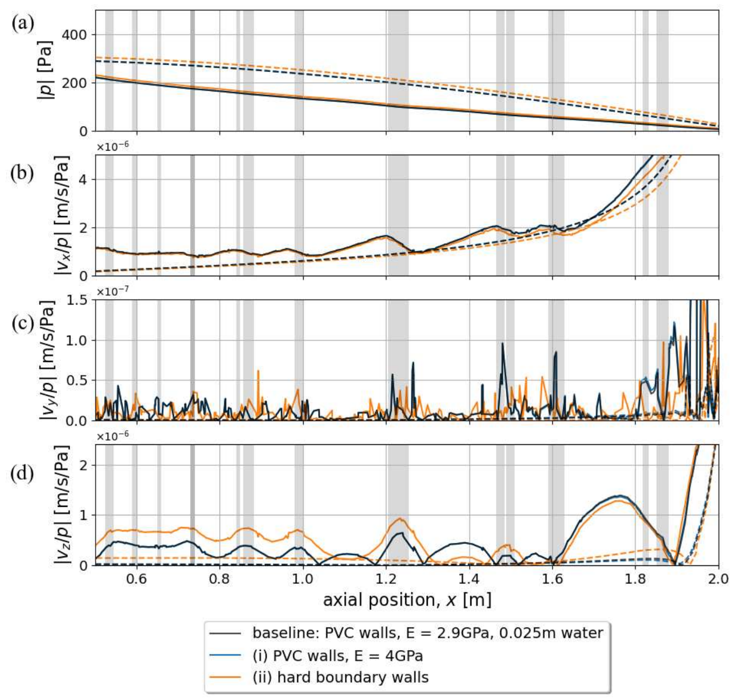

Figure B.17: Comparison of multiple models, similar to the model described in Section 3.2 but with small changes. The results for a defective pipe are shown with solid lines and the complementary results for an intact pipe are shown with dashed lines.

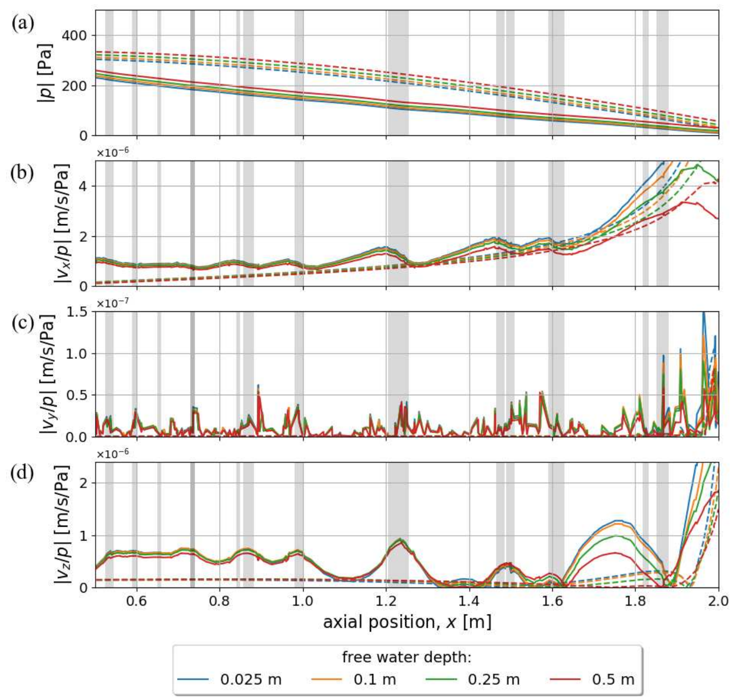

Figure B.18: Comparison of multiple models, similar to the model described in Section 3.2 but with varying water depths. The results for a defective pipe are shown with solid lines and the complementary results for an intact pipe are shown with dashed lines.

References

[1] Water UK. *Design and construction guidance for foul and surface water sewers offered for adoption under the code for adoption agreements for water and sewerage companies operating wholly or mainly in England ('The Code')*, 2019.

[2] P. Rizzo. *Water and wastewater pipe nondestructive evaluation and health monitoring: A review.* Advances in Civil Engineering, 2010, 2010. DOI: 10.1155/2010/818597

[3] Y. Kleiner, B. Adams, and J. Rogers. *Water distribution network renewal planning.* Journal of Computing in Civil Engineering, 15, 2001. DOI: 10.1061/(ASCE)0887-3801(2001)15:1(15)

[4] D. Misiunas. *Failure monitoring and asset condition assessment in water supply systems.* Lund University, Department of Industrial Electrical Engineering and Automation, 2005.

[5] *Technologies to assess conditions of wastewater rising mains.* Water New Zealand Conference Proceedings, 2018. [Online; accessed 5-August-2024].

[6] A. Rainer, T. F. Capell, N. Clay-Michael, M. Demetriou, T. S. Evans, D. A. Jesson, M. J. Mulheron, L. Scudder, and P. A. Smith. *What does NDE need to achieve for cast iron pipe networks?* ICE Infrastructure Asset Management, 4:68–82, 2017. DOI: 10.1680/jinam.16.00020

[7] Y. Yu, A. Safari, X. Niu, B. Drinkwater, and K. V. Horoshenkov. *Acoustic and ultrasonic techniques for defect detection and condition monitoring in water and sewerage pipes: A review.* Journal of Applied Acoustics, 183, 108282, 2021. DOI: 10.1016/j.apacoust.2021.108282

[8] M. S. El-Abbasy, F. Mosleh, A. Senouci, T. Zayed, and H. Al-Derham. *Locating leaks in water mains using noise loggers.* Journal of Infrastructure Systems, 22, 2016. DOI: 10.1061/(ASCE)IS.1943-555X.0000305

[9] Z. Xue, L. Tao, J. Fuchun, E. Riehle, H. Xiang, N. Bowen, and R. P. Singh. *Application of acoustic intelligent leak detection in an urban water supply pipe network*. Journal of Water Supply: Research and Technology-Aqua, 69(5):512–520, 2020. DOI: 10.2166/aqua.2020.022

[10] Pure Technologies, Xylem: SmartBall. https://www.xylem.com/en-us/products--services/pipeline-assessment/smartball-inline-free-swimming-inspection-platform/. Accessed: 2024-08-20.

[11] Pure Technologies, Xylem: Pipediver. https://www.xylem.com/en-us/products--services/pipeline-assessment/pipediver-condition-assessment-platform/. Accessed: 2024-08-20.

[12] Pure Technologies, Xylem: Sahara. https://www.xylem.com/en-us/products--services/pipeline-assessment/sahara-inline-tethered-inspection-platform/. Accessed: 2024-08-20.

[13] Xylem: Increased regulation makes rising main management a risk priority. https://www.xylem.com/en-uk/the-pipeline/assessment-services/increased-regulation-makes-rising-main-management-a-risk-priority/. Accessed: 2024-08-20.

[14] Hong Kong DSD. R&D Report No. RD1074: Assessment of service conditions of rising mains. https://www.dsd.gov.hk/EN/Files/Technical_Manual/RnD_reports/RD201201.pdf. Accessed: 2024-08-20.

[15] N. A. Rodríguez-Olivares, J. V. Cruz-Cruz, A. Gómez-Hernández, R. Hernández-Alvarado, L. Nava-Balanzar, T. Salgado-Jiménez, and J. Alberto J. A. Soto-Cajiga. *Improvement of ultrasonic pulse generator for automatic pipeline inspection.* Sensors, 18(9), 2018. DOI: 10.3390/s18092950

[16] M. M. Gozum, S. Nasraoui, G. Grigoropoulos, M. Louati, and M. S. Ghidaoui, *A noise-based high-resolution time-reversal method for acoustic defect localization in water pipes* Journal of the Acoustics Society of America, 152(6), 3373-3383, 2022. DOI: 10.1121/10.0016502

[17] M. Waqar, M. Louati, and M. S. Ghidaoui, *Time-reversal technique for pipeline defect detection.* Journal of Water Research, 243, 120375, 2023. DOI: 10.1016/j.watres.2023.120375.

[18] C. Xu, M. Waqar, M. Louati, and M. S. Ghidaoui, *High-resolution pipeline leak localization using the side-lobes of the defect detection functional of matched-field processing.* Journal of Mechanical Systems and Signal Processing, 217, 111529, 2024. DOI: 10.1016/j.ymssp.2024.111529.

[19] C. R. Fuller, *The input mobility of an infinite circular cylindrical elastic shell filled with fluid* Journal of Sound and Vibration, 87(3), 409-427, 1983 DOI: 10.1016/0022-460X(83)90470-4

[20] P. M. Morse, K. U. Ingard, *Theoretical Acoustics* Princeton University Press, 1968

[21] COMSOL AB, Stockholm, Sweden. COMSOL Multiphysics® v. 6.2. `www.comsol.com`.

[22] COMSOL documentation: Perfectly Matched Layers. `https://doc.comsol.com/5.5/doc/com.comsol.help.aco/aco_ug_pressure.05.106.html`. Accessed 2025-02-24.

[23] R. Long, P. Cawley, and M. Lowe, *Acoustic wave propagation in buried iron water pipes.* Proceedings of the Royal Society, Part A, 459, 2749-2770, 2003. DOI: 10.1098/rspa.2003.1148.